Supplementary Information

for

Substrate Dependent Exciton Diffusion and Annihilation in Chemically Treated MoS_2 and WS_2

Aaron J. Goodman,[1†] Der-Hsien Lien,[2†] Geun Ho Ahn,[2] Leo L. Spiegel,[3] Matin Amani,[2]

Adam P. Willard,[1] Ali Javey,[2*] William A. Tisdale[3*]

1 – Department of Chemistry, Massachusetts Institute of Technology, Cambridge, MA 02139 United States

2 – Department of Electrical Engineering and Computer Science, University of California Berkeley, Berkeley, CA 94720 United States

3 – Department of Chemical Engineering, Massachusetts Institute of Technology, Cambridge, MA 02139 United States

† equal contribution

* to whom correspondence should be addressed (ajavey@mit.edu; tisdale@mit.edu)

Table of Contents:

I. MoS_2 Absorption Spectra

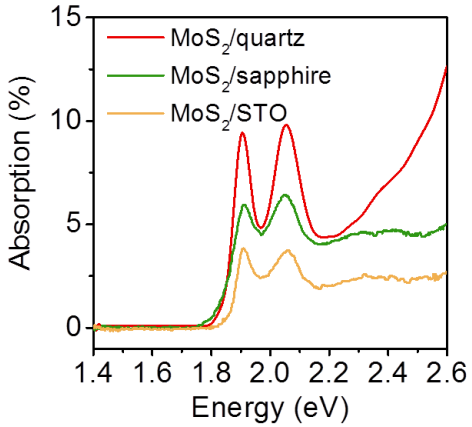

Figure S1 Absorption spectra of MoS_2 supported on quartz (red), sapphire (green), and STO (yellow).

Two measurements were performed to collect the absorption spectra for 2D monolayers on quartz, sapphire and $SrTiO_3$ substrates. In the first measurement, the absolute values of reflection and transmission at a wavelength of 514.5 nm (Ar ion laser) were measured for the extraction of the absorption value using lock-in amplifier coupled with a Silicon photodiode. The extracted absorption values are 7.1%, 4.7% and 2.5% for MoS_2 on quartz, sapphire and STO, respectively. Absorption spectra were obtained using a supercontinuum laser (Fianium WhiteLase SC-400). The reflection/transmission light was analyzed by a spectrometer to produce the spectra. In those measurements, the laser was focused by a 50× objective. For reflection measurement, the reflected light was collected through the same objective. For transmission measurement, the transmitted light was collected using a 20× objective. The system was calibrated using quartz/sapphire/$SrTiO_3$ substrates and silver mirror as the reference for transmission and reflection. Note that the quantum yield, generation rates and exciton concentration (TRPL) are each calculated using the measured absorption.

II. PL Decay Traces

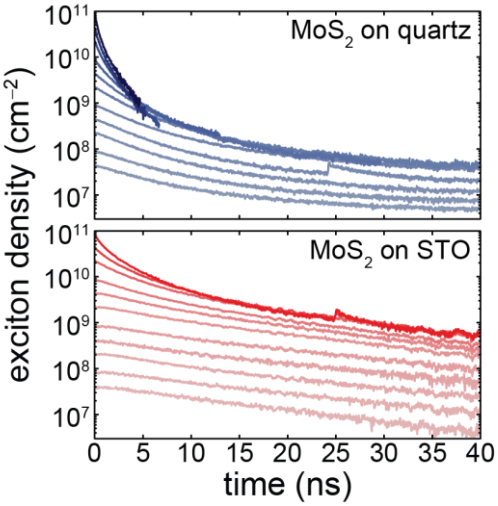

Figure S2 Individual PL decay histograms collected from MoS_2 supported on quartz (top) and STO (bottom). These decay histograms were stitched together and fit with Equation 2 in the main text to extract k_X and k_{XX}.

The individual PL decay histograms exhibit exciton-exciton annihilation at high fluences, which can be seen as a fast component in the PL decay trace. The multi exponential curves are fit by a continuum model in the main text according to Equation 2, reproduced here,

$$\frac{dN(t)}{dt} = -k_X N(t) - k_{XX} N^2(t). \quad \text{(S1)}$$

Such an analysis, as well as stitching together individual traces assumes that the exciton population is "well mixed", that is to say that excitons are randomly distributed throughout the course of the experiment with constant density in the probed focal volume. While this assumption holds to the extent that it is possible to extract key parameters, k_X, *and* k_{XX}, and the curves are well fit by Equation 2, one might not expect the assumption to be strictly true, particularly at high exciton densities. In particular, in the presence of annihilation, surviving excitons develop spatial correlations such that their spatial distribution isn't uniformly distributed and random. They are effectively "anti-bunched". Furthermore, the exciton density is not constant across the experimental excitation profile. However, these details do not affect the fitting of the TCSPC data as confirmed through discrete modelling that showed the continuum modelling holds up under the experimental conditions used here.

III. WS_2 Generation Rate-Dependent Quantum Yield

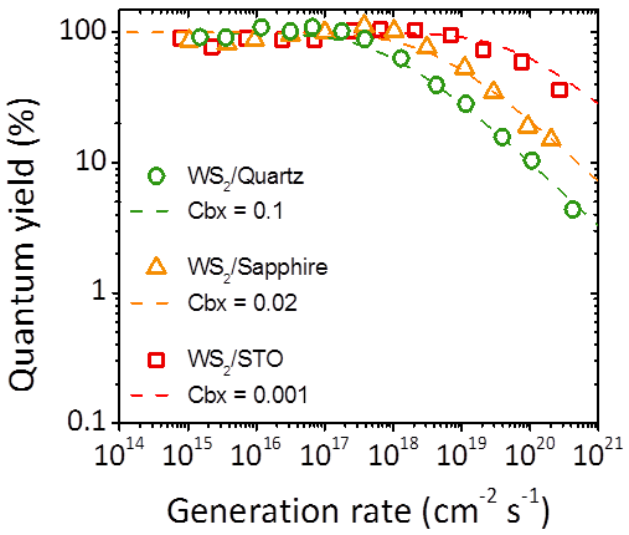

Figure S3 Absolute quantum yield values for WS_2 supported on quartz (green circles), sapphire (yellow triangles), and STO (red squares) extracted from calibrated PL spectra as a function of carrier generation rate. The data are consistent with and qualitatively similar to the data for MoS_2 on the three substrates. At low generation rates, the samples emit with near unity quantum yield. As the generation rate increases, the exciton-exciton annihilation interaction lowers the quantum yield dramatically.

IV. Continuum Model Diffusion Equation

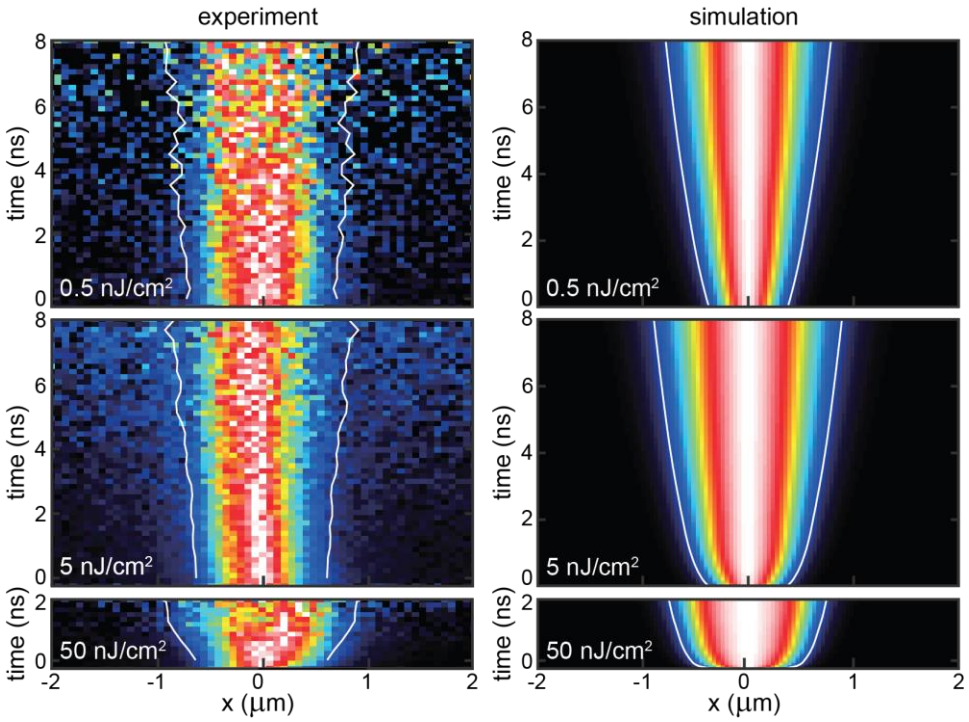

Figure S4 Exciton diffusivity experimental results (left) and continuum modelling (right). Horizontal cuts through the color plots represent normalized line cuts through the Gaussian exciton population spatial distribution as a function of time. White lines track 2σ where σ is the standard deviation of the exciton spatial distribution.

As discussed in the main text, diffusion imaging allows us to visualize the exciton population broadening in time. The experimental results reproduced in the left panels of **Fig. S4** show that the distribution broadens in time due to exciton diffusion and exciton-exciton annihilation. The experimental results are captured by a continuum model that propagates an initial Gaussian exciton population according to

$$\frac{\mathrm{d}N}{\mathrm{d}t} = D\nabla^2 N - (k_{\mathrm{X}} + k_{\mathrm{NR}})N - k_{\mathrm{XX}}N^2, \qquad \text{(S2)}$$

where D is the exciton diffusivity, k_{XX} is the exciton-exciton annihilation rate constant, and k_{X} (the apparent radiative decay rate) and k_{NR} (the nonradiative decay rate) are first order decay rates. The model output (shown in the right panels of **Fig. S4**) agrees with experiment when parameterized with experimentally determined D and k_{XX}.

V. Diffusivity Measurements: Sapphire and STO

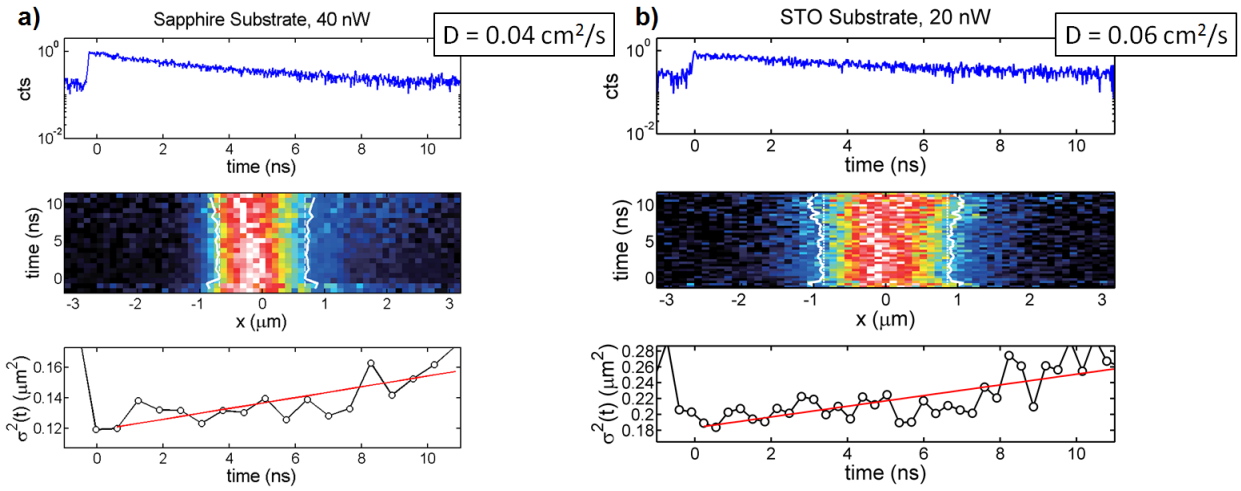

Figure S5 Diffusion imaging experiments performed on MoS_2 supported on sapphire (a), and STO (b). Top panels show the spatially-integrated PL decay. Middle panels show exciton diffusion imaging as discussed in the main text. Bottom panels show the PL spatial distribution variance extracted from the middle panels evolving in time showing diffusive broadening.

Exciton diffusivity measurements were also performed on TFSI-treated MoS_2 transferred to sapphire and STO. In each case the experiment was performed as described in the methods section of the main text at sufficiently low fluence to avoid exciton/exciton annihilation as indicated by the monoexponential PL decay curves shown in the top panels. The PL spatial distribution was fitted to a Gaussian at each time point. The variances from the Gaussian fits are plotted as a function of time in the bottom panel. The variance grows linearly in time at a rate that reflects the diffusivity. In both cases, the measured diffusivity was similar to the diffusivity measured for MoS_2 on quartz: 0.04 ± 0.01 and 0.06 ± 0.02 cm^2/s for MoS_2 on sapphire and STO respectively.

VI. Low Temperature PL Spectra

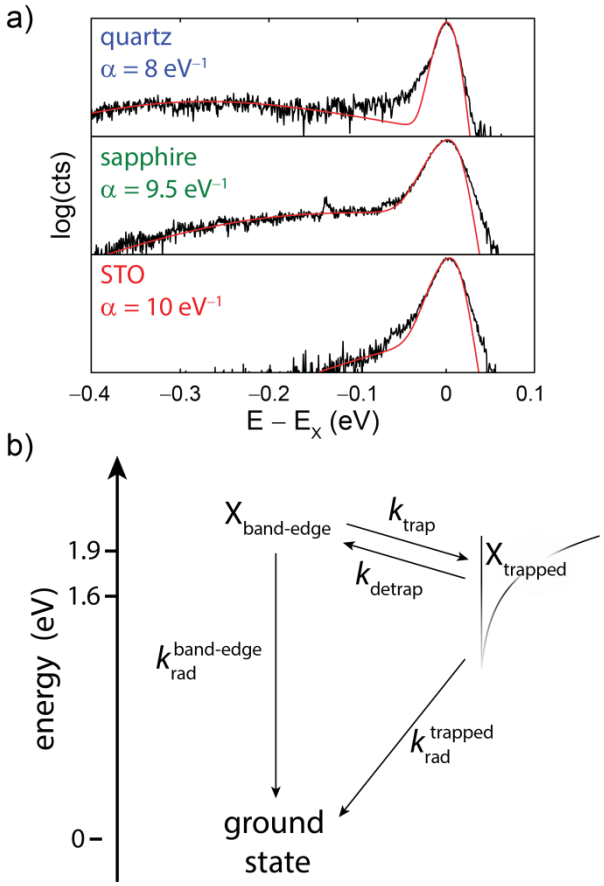

Figure S6. Low-temperature emission spectrum. (a) Log-scale 77 K photoluminescence spectra of MoS_2 supported on quartz (top), sapphire (middle), and strontium titanate (bottom). The photoluminescence spectra (solid black lines) are modelled as a Fermi-Dirac distribution over an exponential density of states (red line). The exponential decay constant, α [eV^{-1}], was extracted from the red line fit to the PL data. (b) Excitonic state diagram for trapped and band-edge (free) excitons.

When the sample was cooled to 77 K, differences in the photoluminescence (PL) spectrum among the three substrates were observed. **Fig. S6a** shows the PL spectra collected at 77 K for TFSI-treated MoS_2 supported on quartz, sapphire, and STO. Note that the original room-temperature PL intensity and spectrum were recovered after the sample was heated from 77 K back to room temperature (see following section). The spectra, which are plotted in **Fig. S6** on a logarithmic scale, exhibit a dominant peak centered at roughly 1.95 eV that is characteristic of band-edge exciton emission, which we will refer to as the "free exciton" feature. The three spectra also exhibit low energy emission below the free exciton, which is not evident in room temperature photoluminescence spectra. These low energy features correspond to slow emission

from long-lived states, which we previously assigned to structural defects in the native MoS_2 crystal.[1] The spectra in **Fig. S6** are successfully fit to a Fermi-Dirac distribution over a Gaussian density of band-edge states plus an exponential tail density of defect states below the band edge, as described graphically in **Fig. S7**. While fitting the spectra, the ratio of the degeneracy of the band edge and trapped exciton states was held constant (*i.e.* we assumed that the trap states were intrinsic to MoS_2 and their density did not depend on the substrate). The energetic distribution of the trap states, parametrized by the exponential decay constant α [eV^{-1}] annotated in the figure, was obtained from fitting the PL spectrum.

The sensitivity of the defect-associated emission to the surrounding dielectric environment and the low oscillator strength of radiative recombination from these states ($\tau_{rad,trap} \sim 10^{-6}$ s)[1] is consistent with a charge-separated exciton state exhibiting weak overlap in the electron-hole wave function. Such states may arise from trapped charges at the oxide interface. However, the monotonic dependence of the trap state distribution on the substrate dielectric constant suggests that the most likely origin of the sub-band PL shown in **Fig. S6** is emission from excitons bound to sulfur site vacancies in the native MoS_2 crystal.

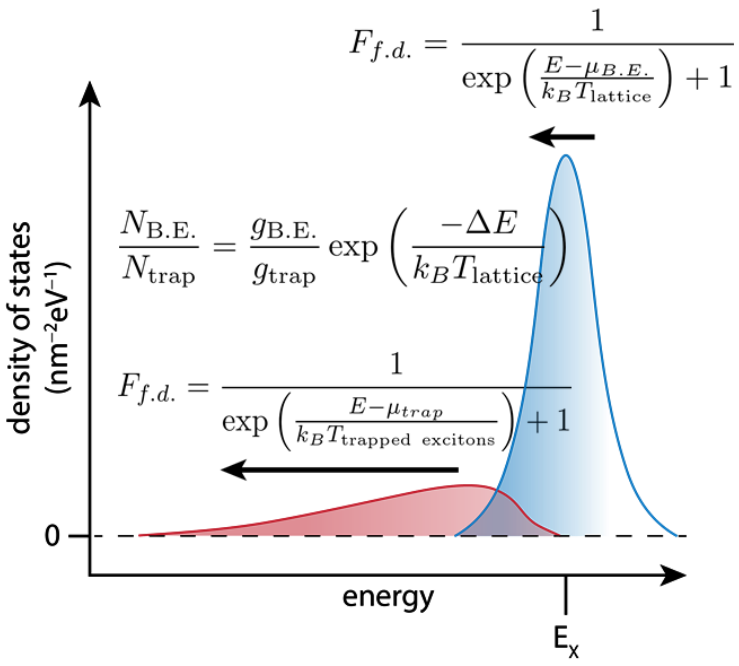

Figure S7 Schematic illustration of the two sub populations that contribute to low-temperature PL spectra.

VII. PL Spectra under Extended Vacuum and Cooling

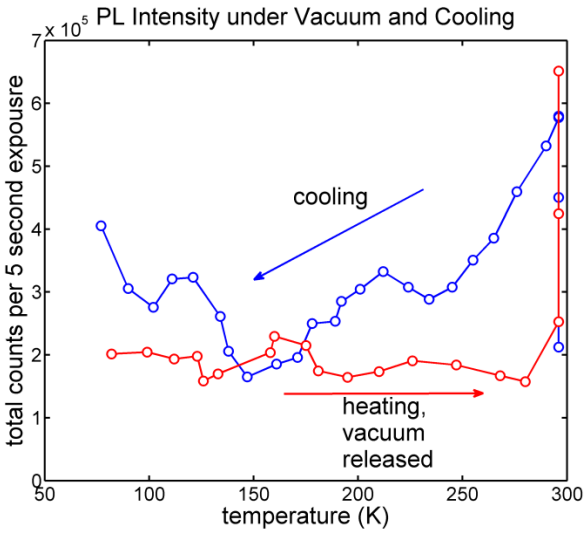

Figure S8 Integrated photoluminescence intensity upon cooling (blue) to and heating (red) from liquid nitrogen temperature. The cooling and heating cycle took approximately one hour.

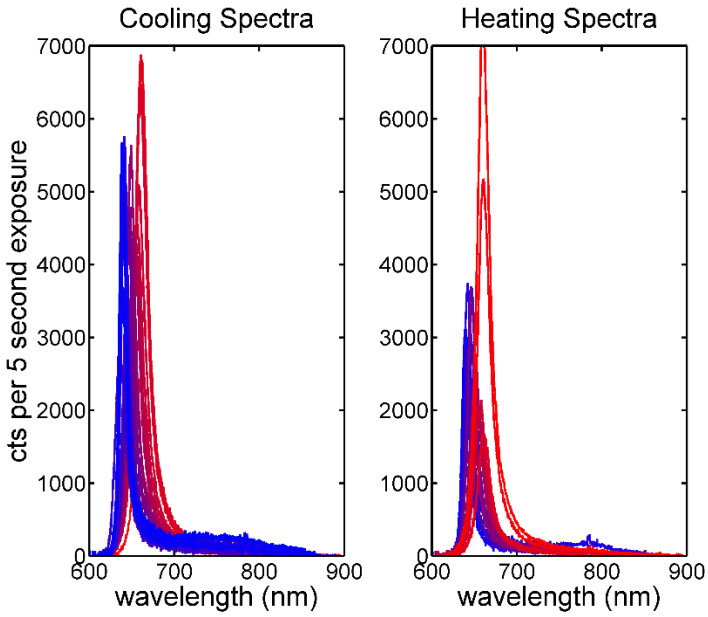

Figure S9 Photoluminescence spectra collected upon cooling (left) to and heating (right) from liquid nitrogen spectra. The color gradation indicates temperature (room temperature is red, 77 K is blue). The cooling and heating cycle took approximately one hour.

To assess the effect of vacuum and low temperature on the polymer-capped samples, the samples were cooled to 77 K and heated to room temperature under vacuum. Upon cooling and concurrent exposure to vacuum, the total PL intensity decreased. Simultaneously, the exciton

emission blue shifted and the red tail of the emission became more prominent. Upon heating, the spectrum red shifted and the emission tail became less prominent again. Notably, the PL intensity recovered only somewhat until the cryostat was returned to atmospheric pressure, at which point the PL intensity completely recovered.

VIII. Monte Carlo Modelling of Experimental Data

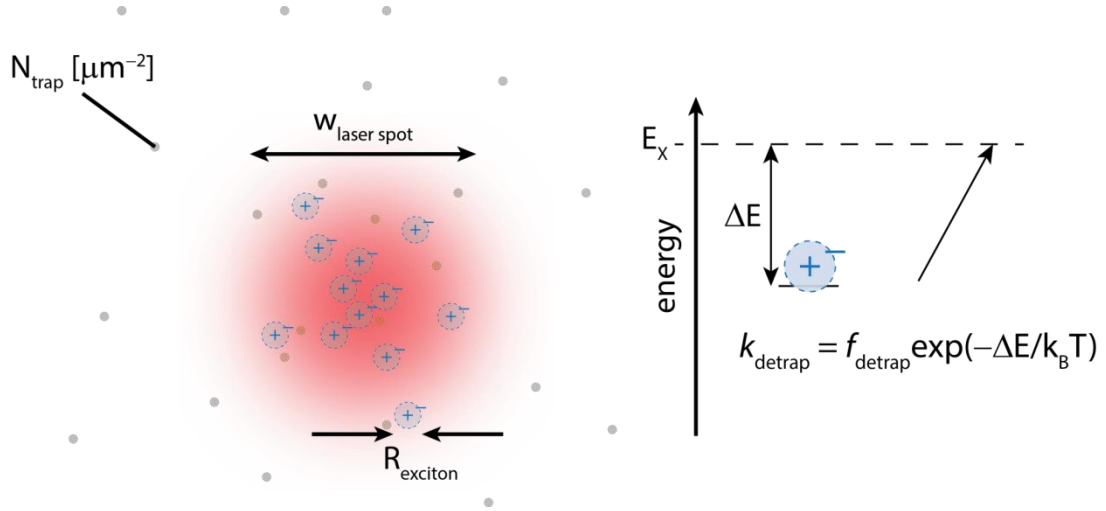

Figure S10 Left: Schematic of the simulation volume. Explicit traps are assigned random locations with an overall density, N_{trap}. Photogenerated excitons are initialized randomly according to the Gaussian intensity profile of the excitation laser. Excitons interact when their centers are separated by $2*R_{\text{exciton}}$. Right: Schematic of the de-trapping process. Each explicit trap is assigned an energy drawn from an exponential tail to free exciton energy as detailed in the accompanying text. Trapped excitons de-trap probabilistically with rate $f_{\text{detrap}} \exp\left(-\frac{\Delta E}{k_{\text{B}}T}\right)$.

Our model describes excitons as mobile particles in a two-dimensional landscape that includes explicit spatially localized traps as shown in **Fig. S10**. Excitons were initialized at the band edge, with a spatial distribution coinciding with that of the focused laser pulse, and then allowed to diffuse in two-dimensions. The dynamics of an exciton persisted until the exciton underwent either radiative decay, simulated stochastically with a rate k_X, or exciton-exciton annihilation, by diffusing within a separation R of another exciton. Exciton trapping and detrapping was simulated using a Monte Carlo algorithm. Namely, when an exciton encountered a trap, it trapped with unity probability and became immobilized. A trapped exciton de-trapped stochastically with a rate determined by the energetic depth of the trap it occupied, as given by,

$$k_{\text{detrap}} = f_{\text{detrap}} \exp\left[-\frac{\Delta E_{\text{trap}}}{k_{\text{B}}T}\right], \tag{S3}$$

where f_{detrap} specifies the base detrapping attempt frequency, ΔE_{trap} denotes the depth of the trap, and $k_{\text{B}}T$ is the Boltzmann constant times temperature. Formulated in this way, the trapping and detrapping rates obey detailed balance. Traps were distributed randomly in space and each trap was assigned a random trapping energy, ΔE_{trap}, distributed on the interval (0.15, 0.4) eV

and weighted by the experimentally-validated exponential distribution $\rho(\Delta E_{\text{trap}}) \propto \exp[-\alpha \Delta E_{trap}]$, where the parameter α was obtained from fitting the low-temperature PL spectrum (**Fig. S6**).

Table S1 Parameters used in the Monte Carlo modelling of exciton diffusion, trapping, and annihilation. The band edge diffusivity ($D_{\text{band edge}}$), trap density, and de-trapping attempt frequency (f_{detrap}) were kept the same for each substrate, while the trap state energy distribution (α) and annihilation radius (R) were substrate-dependent.

	Quartz	Sapphire	STO
$D_{\text{band edge}}$ [cm^2s^{-1}]		5.0	
Trap Density [μm^{-2}]		1000	
f_{detrap} [s^{-1}]		5×10^{13}	
α [eV^{-1}]	6.0	7.5	11
R [nm]	4	0.6	0.4

The model required very few parameters for input, most of which were available from independent experiments. The parameters and their values used in the model are enumerated in **Table S1**. The diffusivity of the freely diffusing band-edge exciton was modelled as $D_{\text{band edge}}$ = 5.0 cm^2s^{-1}. The trapping density was chosen based on the spatial density of charged point defects observed in scanning tunneling microscopy images of exfoliated MoS_2,[2] which reveal a defect density of roughly 1000 per square micron. To reproduce the experimentally measured apparent exciton lifetime (tens of nanoseconds), it was necessary to choose a de-trapping attempt frequency $f_{\text{detrap}} = 5\times10^{13}$ s^{-1}.

There are two critical parameters that depend on the supporting substrate: α, which parameterizes the distribution of trap energies, and R, the radius at which two excitons annihilate. The parameter α, which was obtained from fitting the low-temperature PL spectrum (**Fig. S6**), describes the energetic distribution of the trapping sites and consequently the rate of thermally activated de-trapping from those sites. The second substrate-dependent parameter is the separation, R, at which two excitons annihilate. This parameter is fitted by comparing simulation results to the steady-state QY measurement (Fig. 4b). The fitted values of R depend strongly on the supporting substrate as well: R = 4.0 nm for quartz, R = 0.6 nm for sapphire, and R = 0.4 nm for STO. As the refractive index of the substrate is increased, the separation, R, at which excitons interact apparently decreases. This is consistent with exciton-exciton annihilation

mechanisms that require electron wavefunction overlap, or interaction *via* Coulomb or dipole interactions, both of which would be modulated by the surrounding dielectric environment, with less screening (*i.e.* lower index) favoring more distant interactions (*i.e.* larger *R*). However, we emphasize that the value of *R* may also be interpreted as an annihilation cross-section that does not have direct meaning as a physical distance of interaction.

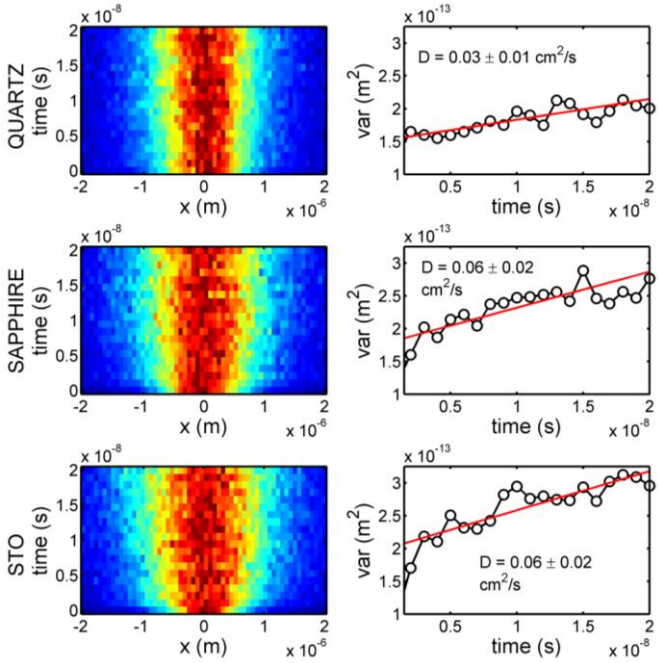

Figure S11 Monte Carlo simulation of time- and spatially-resolved emission microscopy data. The Left column plots the simulated exciton diffusion imaging experiment. The right column plots the variance of the Gaussian spatial profile as a function of time. The fitted diffusivities are labeled in the inset. The model predictions are plotted for MoS_2 on quartz (top row), sapphire (middle row), and STO (bottom row).

The output of the Monte Carlo model is plotted along with the experimental steady-state QY data in **Fig. 4b**; the values of k_{XX} predicted by the model are plotted with the experimentally determined values in **Fig. 4c**. The model accurately reproduces the steady-state experiments. Importantly, the model also reproduces the annihilation dynamics and transport behavior observed in the transient experiments (**Fig. S11** & **S12**). Our Monte Carlo model with explicit excitons and traps accurately reproduces the experimental diffusion imaging data (**Fig. S11**) using a free exciton band edge diffusivity of 5 cm^2/s. As seen in the main text (**Fig. 2**) and shown in the model results (**Fig. S11**), the experimentally observed diffusivity (D = 0.06 cm^2/s) may be

orders of magnitude lower than the diffusivity of the freely-diffusing band-edge exciton (D = 5 cm^2/s) when exciton trapping is considered.

Furthermore, the Monte Carlo model accurately reproduces the experimental PL decay dynamics. The band edge radiative rate is set to $(900\ ps)^{-1}$, which is much faster than the experimentally measured effective lifetime due to equilibration between band edge excitons and trapped excitons. The transient simulation also accurately captures exciton annihilation, which is most prominent on quartz. There is evidence of annihilation in simulated fluences as low as 5 excitons per μm^2.

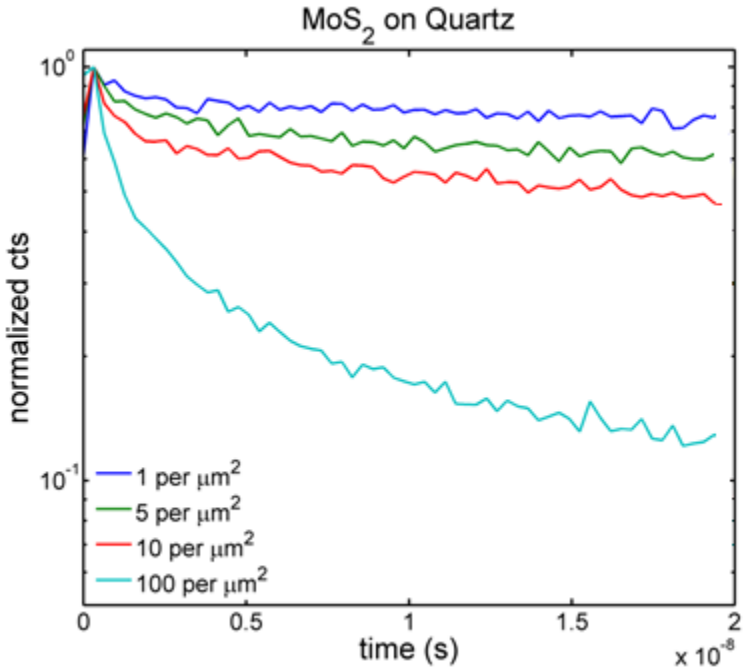

Figure S12 Simulated transient PL decay traces. The Monte Carlo simulation predictions for fluences of 1 (blue), 5 (green), 10 (red), and 100 (cyan) excitons per μm^2 are normalized and plotted. The simulated sample is MoS_2 on quartz.

Simulation Methods

Steady-State Quantum Yield Implementation

The steady-state quantum yield for a given generation rate, R_{gen}, is modelled as follows:

1) The simulation box is populated with traps with a prescribed area density, N_{trap}, and an exponentially decaying energetic distribution, $\rho \propto \exp[-\alpha(E - E_{band\ edge})]$, where the parameter α is extracted from low temperature PL spectra.
2) The simulation box is populated with free excitons with rate R_{gen} following the Gaussian intensity profile of the excitation laser.
3) Free excitons diffuse with the band edge diffusivity and decay with the band edge radiative rate.
    a. If a free exciton encounters an empty trap, it traps.
    b. If a free exciton encounters a trapped exciton, it annihilates.
    c. Trapped excitons detrap with rate $f_{\mathrm{detrap}} \exp\left(-\frac{\Delta E}{k_B T}\right)$.
4) The number of emitted photons is divided by the number of generated excitons to extract the quantum yield.

Transient TCSPC Implementation

The transient simulations are performed for fixed initial exciton density, $N(t = 0)$. These simulations yield simulated diffusivities, D, and transient PL traces.

1) The simulation box is populated with traps with a prescribed area density, N_{trap}, and an exponentially decaying distribution with energy $\rho \propto \exp[-\alpha(E - E_{band\ edge})]$, where the parameter α is extracted from low temperature PL spectra.
2) The simulation box is populated with $N(0)$ excitons following the Gaussian intensity profile of the excitation laser.
3) Free excitons diffuse with the band edge diffusivity and decay with the band edge radiative rate.
    a. If a free exciton encounters an empty trap, it traps.
    b. If a free exciton encounters a trapped exciton, it annihilates.
    c. Trapped excitons detrap with rate $f_{\mathrm{detrap}} \exp\left(-\frac{\Delta E}{k_B T}\right)$.
4) Whenever a free exciton decays radiatively, its emission time and spatial location are recorded. The emission times are histogrammed to model transient PL decay curves. The locations can be plotted to reproduce diffusion imaging experiments.

IX. Supplementary References

1. Goodman, A. J.; Willard, A. P.; Tisdale, W. A. Exciton Trapping is Responsible for the Long Apparent Lifetime in Acid-Treated MoS_2. *Phys. Rev. B* **2017**, *96*, 121404.
2. Amani, M.; Taheri, P.; Addou, R.; Ahn, G. H.; Kiriya, D.; Lien, D.-H.; Ager, J. W.; Wallace, R. M.; Javey, A. Recombination Kinetics and Effects of Superacid Treatment in Sulfur- and Selenium-Based Transition Metal Dichalcogenides. *Nano Lett.* **2016**, *16*, 2786-2791.